Fixed target measurements at LHCb for cosmic rays physics

GIACOMO GRAZIANI
INFN, Sezione di Firenze, via Sansone 1, 50019 Sesto Fiorentino (FI), Italy

The LHCb experiment has the unique possibility, among the LHC experiments, to be operated in fixed target mode, using its internal gas target. The energy scale achievable at the LHC, combined with the LHCb forward geometry and detector capabilities, allow to explore particle production in a wide Bjorken-x range at the $\sqrt{s_{\rm NN}} \sim 100$ GeV energy scale, providing novel inputs to nuclear and cosmic ray physics. The first measurement of antiproton production in collisions of LHC protons on helium nuclei at rest is presented. The knowledge of this cross-section is of great importance for the study of the cosmic antiproton flux, and the LHCb results are expected to improve the interpretation of the recent high-precision measurements of cosmic antiprotons performed by the space-borne PAMELA and AMS-02 experiments.

1 LHCb as a fixed target detector

The LHCb detector [1] is a single-arm forward spectrometer covering the pseudorapidity range $2 < \eta < 5$, designed for the study of particles containing b or c quarks, which are predominantly produced at high η in pp collisions at the LHC. The forward geometry and excellent vertexing, tracking and particle identification (PID) capabilities [2], which are key features for the reconstruction of heavy flavour decays, make it also an ideal tool to study interactions of the LHC beams with a fixed target. Such target is provided by the SMOG (System for Measuring Overlap with Gas) device [3,4], through which tiny amounts of a noble gas (He, Ne, Ar) can be injected inside the primary LHC vacuum around the LHCb vertex detector (VELO). The design gas pressure in the VELO region is 2×10^{-7} mbar, which is small enough not to significantly perturb the LHC operation. The device was originally conceived to determine the machine luminosity using a beam gas imaging technique[4]. Since 2015, LHCb has started to exploit SMOG to perform a set of physics runs, using special fills not devoted to pp physics, with different beam and target configurations, allowing a wealth of unique production studies. One of the main goals of this program is the study of heavy flavour production in proton-ion collisions with different target mass number at $\sqrt{s_{\rm NN}} \sim 100$ GeV, an intermediate energy between the existing data collected at SPS and RHIC/LHC accelerators. These measurements can shed light on the cold nuclear matter effects affecting the production of the most relevant probes that are used for detecting quark-gluon plasma at higher energy density. Another attractive feature of the fixed target configuration is the access to the large Bjorken-x region in the target nucleus. Nuclear PDFs in this region are sensitive to antishadowing effects and to possible contributions from intrinsic charm and beauty. The first results for charm production, obtained from a data set of proton-argon collisions at $\sqrt{s_{\rm NN}} = 110$ GeV corresponding to a few nb^{-1}, have been recently released [?]. Though the results are still limited by the data size, the observed differential D^0 and J/ψ yields are already expected to provide constrains on nuclear PDFs at large x. Exclusive particle production studies in this kinematic range can also provide crucial inputs to the modelling of cosmic ray showers in the atmosphere and in the cosmos.

2 Cosmic collisions at LHCb

The measurement discussed in the following is motivated by the high-precision determination of the $\overline{p}/p$ ratio in cosmic rays, up to the energy of 350 GeV, achieved during the last years by the space-borne PAMELA [6] and AMS-02 [7] experiments. The investigation of the antimatter content in cosmic rays is recognized as a primary tool for the understanding of high-energy astrophysical phenomena and the measurements of the antiproton fraction outside of the Earth's atmosphere provides a sensitive indirect probe for Dark Matter. The interpretation of these measurements is currently limited by the uncertainty on the expected amount of secondary antiprotons produced by spallation of primary cosmic rays on the interstellar medium. State-of-the-art calculations [8,9,10] show that the experimental results are still compatible with the secondary $\overline{p}$ production, tough data indicate a larger $\overline{p}$ flux at high energy with respect to most predictions. The largest uncertainty on the prediction is due, particularly in the 10–100 GeV range, to the limited knowledge of the $\overline{p}$ production cross-section in the relevant processes. In particular, no data for $\overline{p}$ production exist for pHe collisions.

3 Measurement of antiproton production in pHe collisions

LHCb performed the first measurement of $\overline{p}$ production in pHe collisions by operating SMOG with helium during special fills with limited number of proton bunches, accelerated to 6.5 TeV ($\sqrt{s_{\rm NN}}$ =110 GeV). Most of the data were collected in a single LHC fill during about five hours in May 2016. Events were triggered with a minimum bias requirement, fully efficient on the collisions producing an antiproton within the detector acceptance. The measurement is performed from collisions occurring in an 80 cm long fiducial region, where the best reconstruction efficiency is achieved. Antiprotons are counted in two-dimensional bins in momentum (p) and transverse momentum ($p_{\rm T}$), in the range $12 < p < 110$ GeV/c, $0.4 < p_{\rm T} < 4$ GeV/c. The kinematic limits are dictated by the acceptance of the two ring-imaging Cherenkov detectors (RICH) providing particle identification. The first one covers the range $2 < \eta < 4.4$ and allows $\overline{p}/K^-$ separation in the momentum range 10-60 GeV/c, while the second has acceptance $3 < \eta < 5$ and actively identifies antiprotons between 30 and about 110 GeV. The analysis described in this document covers only the prompt $\overline{p}$ production, namely the antiprotons produced directly in the pHe collision, or from resonances decaying via the strong interaction. The component due to hyperon decays, treated here as a background component and subtracted from the result, will be the subject of a dedicated study.

3.1 Reconstruction

Candidates are selected by requiring a negative track in the kinematic range of interest after applying quality requirements on the reconstruction of the track and of the collision primary vertex (PV), whose position must be compatible with the beam geometry and lie within a 80 cm long fiducial region where the best reconstruction efficiency is achieved. These requirements are almost fully efficient in simulation, while allowing to suppress vertices from decays, secondary collisions, or combinatorial track association in events produced by collisions occurring upstream of the fiducial region. The PV reconstruction efficiency is estimated from simulation. The average value varies with z from 76% in the most upstream region to 95% around the nominal collision point, with a mild dependence on the $p_{\rm T}$ of the candidate $\overline{p}$. The related systematic uncertainty is evaluated by weighting the simulation to account for discrepancies in the PV topology description with respect to data. The reconstruction efficiency for prompt antiprotons, $\epsilon_{\rm rec}$, including acceptance effects and the tracking detector efficiency, is determined from simulation in three-dimensional bins of p, $p_{\rm T}$ and z. The bins are chosen to be small enough to minimize the dependence on the assumed spectra in simulation, but are at least five times larger than the resolution in each variable. The size of the kinematic bins is chosen according to the

expected spectrum of reconstructed antiprotons, while twelve bins of equal size are used for z. To control systematic uncertainties, only bins where $\epsilon_{\rm rec}$ exceeds 35% are retained. The tracking efficiency predicted by the simulation, averaged over z, ranges from 40 to 80% depending on the track kinematics. A correction determined from calibration samples in pp data, of order 1%, is applied to account for imperfections in the simulation of the tracking detector response.

3.2 Particle identification

Antiprotons within the selected sample of negative tracks are identified through the response of the RICH detectors, from which two variables are built, DLL($\mathrm{p}-\pi$) and DLL($\mathrm{p}-\mathrm{K}$), representing the difference of the log likelihood between the proton and pion and the proton and kaon hypothesis. The fraction of antiprotons among the negative tracks is determined from the two-dimensional distribution of the DLL variables. Three sets of templates for the different particles species are considered: predicted by the simulation, obtained from calibration samples in the pHe data set, and from calibration samples in the LHCb pp data collected in 2016. The pHe calibration samples consist of selected $K^0_{\rm S} \to \pi^+\pi^-$ decays for pions, $\Lambda \to p\pi^-(\overline{\Lambda} \to \overline{p}\pi^+)$ for (anti)protons and $\phi \to K^+K^-$ for kaons. Calibration samples in pp data have much larger size, and, thanks to the available $D^{*\pm} \to D^0(K^\mp\pi^\pm)\pi^\pm$ selection, provide better coverage of the region with high p and $p_{\rm T}$ for kaons. On the other hand they are characterized by a much larger detector occupancy, which is critical for the RICH performance, with respect to the pHe events. Such difference is taken into account by weighting the pp events according to the observed charged track multiplicity. The most appropriate calibration templates are chosen for each kinematic region, while the related systematic uncertainty is estimated from their comparison. The fraction of antiprotons in each kinematic bin of the selected sample is determined with a two-dimensional extended binned maximum likelihood fit, where the (DLL($\mathrm{p}-\pi$), DLL($\mathrm{p}-\mathrm{K}$)) distribution in data is fitted as the sum of four components: π^-, K^-, $\overline{p}$ and ghost tracks. The latter component, whose template is obtained from simulation, is needed to account for candidate tracks which can not be unambiguously matched to a particle. This occurs in simulation in about 2% of cases. The DLL distributions for data and calibration samples, illustrating the RICH performance, are shown in Fig. 1 for an arbitrary kinematic bin.

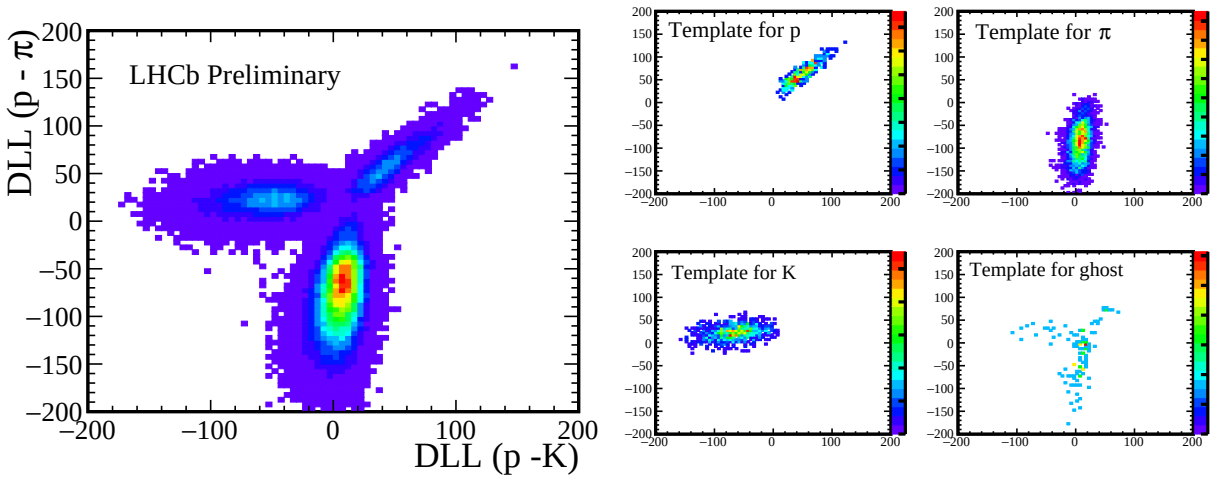

Figure 1 – Example of two-dimensional DLL distributions for a particular bin ($21.4 < p < 24.4\,\mathrm{GeV}/c, 1.2 < p_{\rm T} < 1.5\,\mathrm{GeV}/c$), illustrating the performance of the RICH detectors in separating π^-, K^- and $\overline{p}$ particles. The distribution in data is shown on the left, while the templates for the four categories, obtained from calibration samples (from simulation for the ghost component), are shown on the right.

3.3 Backgrounds

The selected antiprotons that are not prompt are treated as a background and are subtracted from the selected sample. Such background is suppressed by requiring that the impact parameter (IP), which is reconstructed through the VELO with a resolution of $(15 + 29/p_{\mathrm{T}}(\,\mathrm{GeV}/c))$ μm, is compatible with zero. The residual nonprompt background varies in simulation between 3% at the lowest p_{T} values and 1% at high p_{T}. In 90% of cases, this background is due to hyperon decays, while in the remaining cases the antiprotons come from a secondary collision in the detector material and are mistakenly assigned to the primary vertex. The average background level is constrained from the tail of the IP distribution in data to be $(2.6 \pm 0.6)\%$, where the uncertainty is systematic and is estimated by varying the fraction of nonprompt $\overline{p}$ in simulation within the range where a good agreement with data is observed.

Another background to be considered is due to the possible contamination of the gas target. The rate of collisions on the LHC residual vacuum is evaluated by acquiring part of the data without the injected helium gas, while using the same vacuum-pumping configuration of the data taking with gas. The yield measured in these special data are scaled according to the corresponding number of protons on target, and the relative average contribution from residual vacuum is evaluated to be $(0.7 \pm 0.2)\%$, where the uncertainty is systematic. In Fig. 2, the normalized PV multiplicity distributions for data with and without injected gas are compared. The multiplicity is slightly lower on average for the collisions on the residual gas, though it exhibits a longer tail. This confirms that residual vacuum is dominated by hydrogen, with a small contribution from elements heavier than helium, as indicated by the rest gas analysis performed by the LHC vacuum group in the absence of beam.

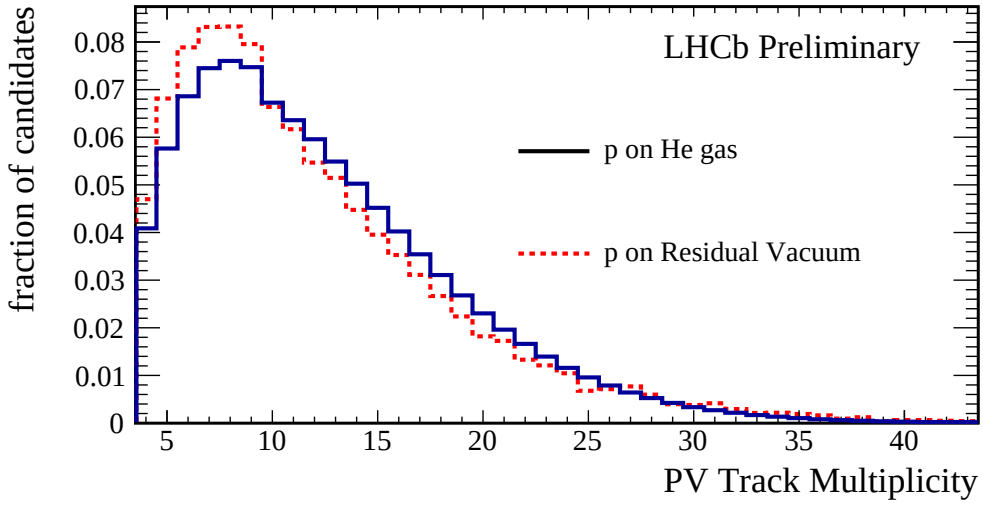

Figure 2 – PV track multiplicity distributions for collisions on residual vacuum or on the helium target.

3.4 Normalization

The SMOG device does not presently allow a precise calibration of the injected gas pressure. Instead, the normalization for the $\overline{p}$ production measurement is provided by observing a process with a well-known cross-section. Single electrons scattered off by the proton beam can be observed within the LHCb acceptance. For a 6.5 TeV proton beam, in the corresponding kinematic range the scattering is purely elastic. The cross-section in the polar angle range $3 < \theta < 27$ mrad, outside of which the electrons can not be reconstructed in LHCb, is 180.6 μb. Though this is three orders of magnitude below the total nuclear inelastic cross-section, events are expected to have a distinct signature, with a single low-momentum and low-p_{T} electron track visible in the detector, with little or no other activity. Background events which could mimic this signature

are expected from soft nuclear interactions where the candidate electron is either the product of a photon conversion, or a light hadron from a central exclusive production event. In both cases the background is charge symmetric. This allows to model the background from events with a single positively charged track (referred to as single positrons in the following). Multiplicity distributions in data confirm that background-dominated regions close to the signal are charge symmetric.

Single electrons candidate events are selected through a loose kinematic selection on the track and applying veto requirements on any detector activity not compatible with the elastic scattering hypothesis. The selection yields 16569 single e^- candidates and 9548 e^+ candidates. The signal yield is obtained by the difference of the two components. The background subtracted kinematic distributions are shown on Fig. 3. An excellent agreement with the simulation is observed, confirming the validity of the charge-symmetry hypothesis for the background.

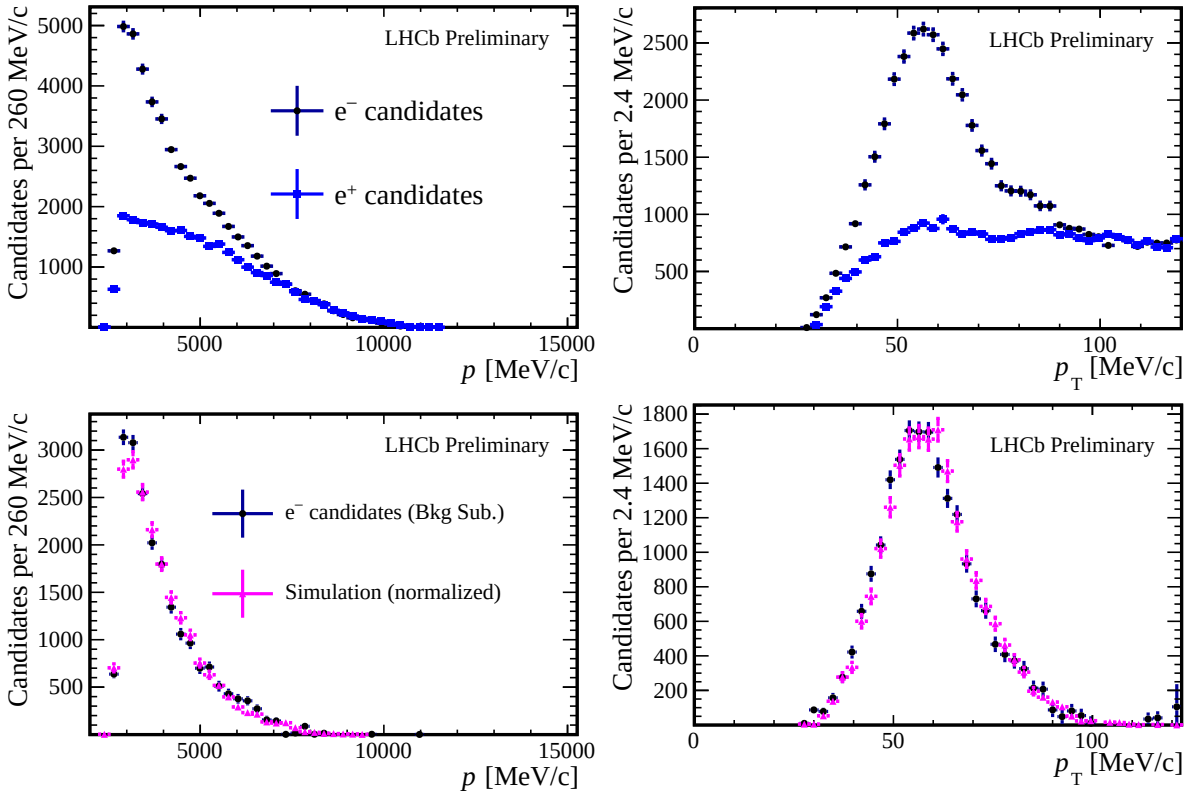

Figure 3 – Distributions of (left) momentum and (right) $p_{\rm T}$ for (top plot) single electron and single positron candidates; (bottom plot) background subtracted electron candidates, compared with the distributions in simulation, which are normalized to data.

The luminosity is determined from the background-subtracted yield of scattered electrons N_e, the known cross-section σ_{pe^-} and the electron reconstruction efficiency $\epsilon_{\rm e}$, as $\mathcal{L} = N_e/(Z_{He} \times \sigma_{pe^-} \times \epsilon_{\rm e})$, where $Z_{He} = 2$ is the helium atomic number. Possible effects of gas ionization were evaluated and are expected to be negligible. The reconstruction efficiency, evaluated from simulation, is limited by the soft momentum and transverse momentum spectrum. Electrons lose a sizable fraction of their energy through bremsstrahlung in the beam pipe and detector material, and large acceptance effects are caused by the spectrometer magnetic field. The relative systematic uncertainty on $\epsilon_{\rm e}$ is estimated to be 6% from the stability of the result when varying the main selection criteria, and in particular from the ability of the simulation to describe the large modulation of the efficiency with the electron azimuthal angle. The result is $\mathcal{L} = 0.443 \pm 0.011 \pm 0.027$ nb^{-1}, where the first uncertainty is statistical, and the second is systematic, dominated by the uncertainty on $\epsilon_{\rm e}$.

Table 1: Relative uncertainties on the $\overline{p}$ production cross-section measurement. The ranges refer to the variation among kinematic bins.

Source	Statistical	Systematic (correlated)	Systematic (uncorrelated)
Data size	$0.7 - 10.8\%$ ($< 3\%$ for most bins)		
Normalization	2.5%	6.0%	
Event and PV requirements		0.3%	
PV reco		0.8%	
Tracking		2.2%	3.2%
Nonprompt background		$0.3 - 0.7\%$	
Residual vacuum background		0.1%	
Efficiency of IP requirement			1.0%
PID		$1.2 - 5.0\%$	$0 - 26\%$ ($< 10\%$ for most bins)
Simulated sample size			$0.8 - 15\%$ ($< 4\%$ for $p_{\rm T} < 2$ GeV/c)

3.5 Uncertainties

Table 1 summarizes the uncertainties on the cross-section measurement. The precision of the measurement is limited by the systematic uncertainty. The largest uncertainty which is correlated among all kinematic bins is the aforementioned relative 6% on the normalization. The uncorrelated uncertainty is dominated for most bins by the error on the $\overline{p}$ fraction from the PID analysis. Large relative uncertainties, up to 26%, affect the bins at the borders of the detector acceptance and, for the intermediate momentum region, in the transition region between the two RICH detectors, at $\eta \sim 4.4$. For the other regions, the accuracy is typically a few per cent. The relative total uncertainty in each bin is illustrated in Fig. 4. It amounts to a relative 10% or less for most of the accessible $p_{\rm T}$ regions.

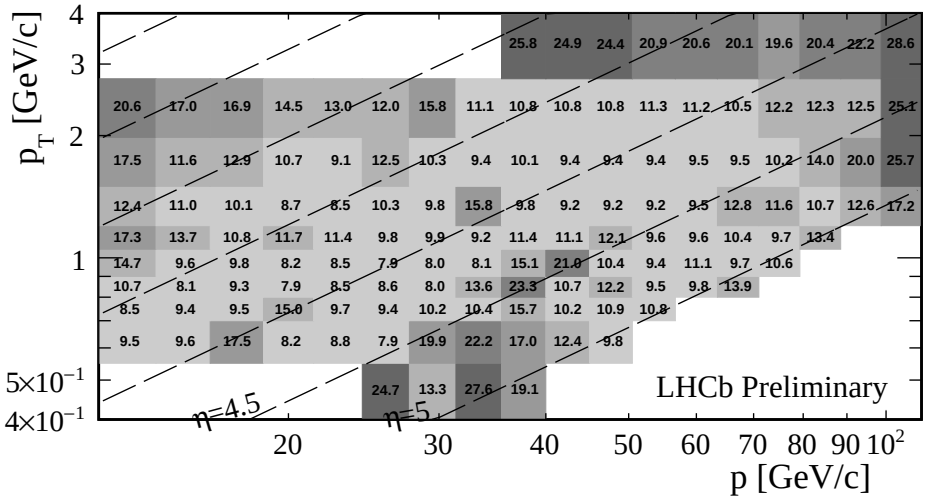

Figure 4 – Total relative uncertainty for the cross-section measurement in each kinematic bin, in per cent.

A major difference between the fixed target configuration and the standard pp data taking in LHCb is the extension of the luminous region. Particular care is devoted to evaluate the dependence on the z of the different experimental effects. The $\overline{p}$ yield normalized to the electron yield is found to be independent of z within the statistical uncertainty. The stability of the result is also checked as a function of the absolute time and of the time within the LHC orbit, excluding unexpected biases related to the beam time structure.

3.6 Results

The antiprotons candidates are counted from a sample of 33.7 million selected pHe collisions, from which a sample of 1.4 million antiprotons is determined by the PID analysis. The double differential $\overline{p}$ production cross-section $d^2\sigma/dp\,dp_{\rm T}$ is computed in each kinematic bin after correcting for the reconstruction efficiency and the background. The results are compared in Fig. 5 with the predictions of the EPOS LHC [11] model, which is used in the LHCb simulation.

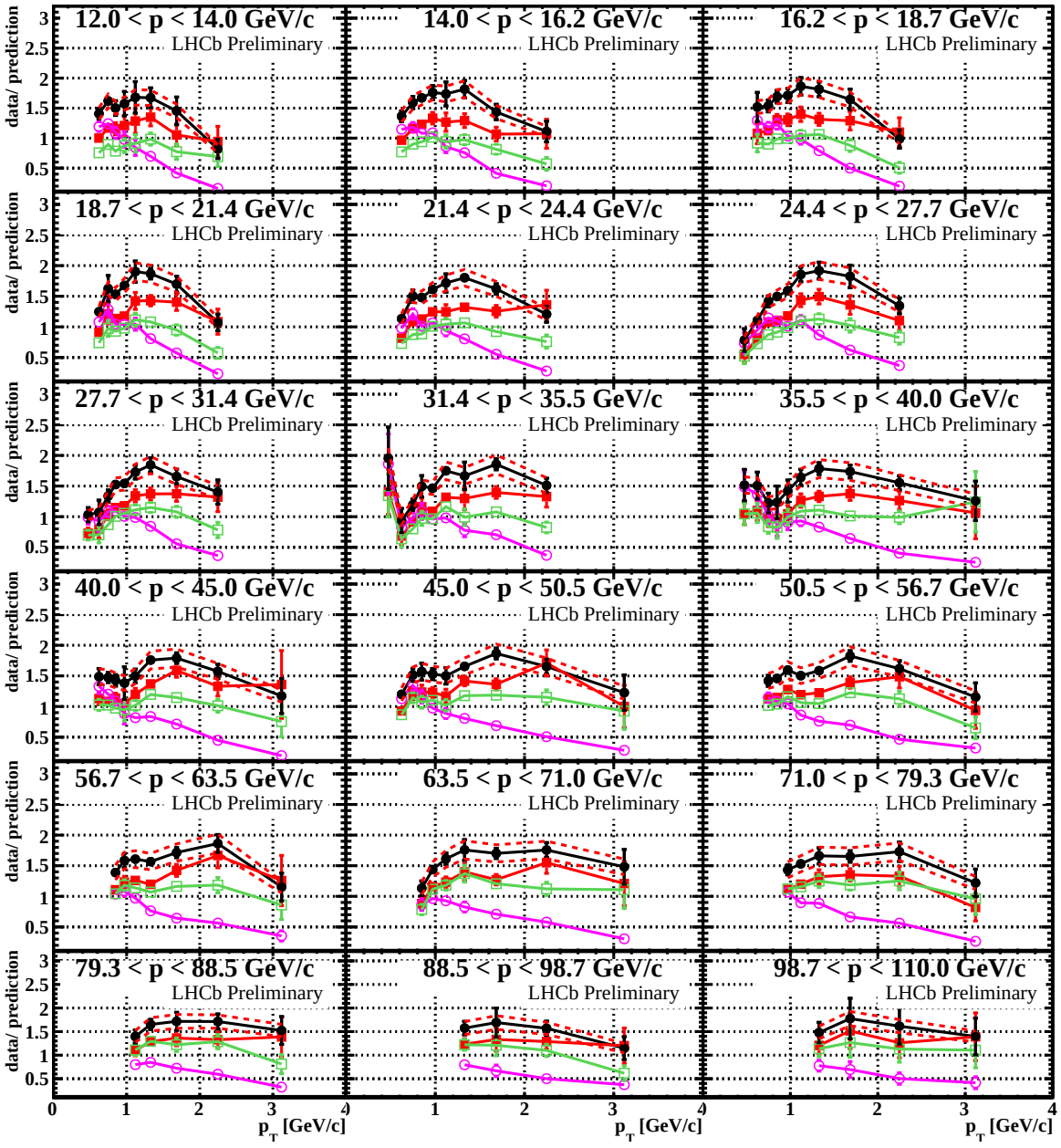

Figure 5 – Result for the $\overline{p}$ cross-section measurement, compared to absolute predictions from different models. The plots show the ratio of data over simulation as a function of $p_{\rm T}$ in the 18 momentum bins, for (black round closed symbols) EPOS LHC, (red squared closed symbols) EPOS 1.99, (green squared open symbols) HIJING 1.38, and (violet round open symbols) QGSJETII-04. The error bars represent the uncorrelated uncertainty for each measurement. The additional correlated uncertainty, shown only for EPOS LHC but also relevant to the other cases, is indicated by the red dashed lines.

The double differential shape, notably the momentum spectrum, is found to be in good agreement with the simulation, while the absolute production rate is larger on average by about a factor 1.5. The data are also compared with three other models implemented in the CRMC [12] package v1.5.6: EPOS 1.99 [13], HIJING 1.38 [14] and QGSJET II-04 [15].

The total inelastic cross-section is also determined from the measured total yield of recorded collisions within the fiducial region. The PV reconstruction efficiency for inelastic collisions is predicted, assuming the EPOS LHC model, to be $56.4 \pm 2.0\%$. The result is $\sigma_{\text{inel}}^{\text{LHCb}}(p\text{He}, \sqrt{s_{\text{NN}}} = 110\,\text{GeV}) = (140 \pm 10)$ mb which is larger than the EPOS LHC prediction by a factor 1.19 ± 0.08, implying that the measured $\overline{p}$ multiplicity per inelastic collision is significantly larger in data. The multiplicity predicted by the pre-LHC version of EPOS is in better agreement with data. HIJING predicts a lower inelastic cross-section (100 mb), while it reproduces well the measured absolute $\overline{p}$ production cross-section values. QGSJET matches the measured values at very low p_{T}, while it exhibits a harder p_{T} spectrum than data.

4 Conclusions and Outlook

The LHCb experiment has recently opened the way to the use of the LHC beams for fixed target physics. The first measurement of antimatter production in pHe collisions is one of the first results of this novel program. Further details on this work can be found in the related LHCb conference contribution [16]. The results are expected to contribute to reduce the uncertainty on the prediction for the secondary antiproton flux in cosmic rays. Further development of this study in the near future is foreseen, with the inclusion of data collected at $\sqrt{s_{\text{NN}}} = 86.6$ GeV during November 2016, and the measurement of the contribution due to hyperon decays. Several other measurements relevant to the modelling of cosmic ray interactions will be possible in the near future: production of light charged particles, including deuterons, photons and charmed particles with different gas targets.

Acknowledgments

We are indebted to our colleagues from the cosmic ray community, O. Adriani, L. Bonechi, F. Donato and A. Tricomi, who suggested this measurement, and would like to thank F. Donato and T. Pierog for their advice.

References

1. LHCb collaboration, A. A. Alves Jr. *et al.*, JINST **3** (2008) S08005
2. LHCb collaboration, R. Aaij *et al.*, Int. J. Mod. Phys. **A30** (2015) 1530022
3. C. Barschel, PhD thesis, RWTH Aachen U., 2014, Presented 05 Mar 2014
4. LHCb collaboration, R. Aaij *et al.*, JINST **9** (2014) P12005
5. LHCb collaboration, CERN-LHCb-CONF-2017-001
6. PAMELA collaboration, O. Adriani *et al.*, JETP Letters **96** (2013) 621
7. AMS collaboration, M. Aguilar *et al.*, Phys. Rev. Lett. **117** (2016) 091103
8. M. di Mauro, F. Donato, A. Goudelis, and P. D. Serpico, Phys. Rev. **D90** (2014) 085017
9. G. Giesen *et al.*, JCAP **09** (2015) 023
10. R. Kappl, A. Reinert, and M. W. Winkler, JCAP **10** (2015) 034
11. T. Pierog *et al.*, Phys. Rev. **C92** (2015) 034906
12. T. Pierog, C. Baus, and R. Ulrich, web.ikp.kit.edu/rulrich/crmc.html
13. T. Pierog and K. Werner, Nucl. Phys. Proc. Suppl. **196** (2009) 102
14. M. Gyulassy and X.-N. Wang, Comput. Phys. Commun. **83** (1994) 307
15. S. Ostapchenko, Phys. Rev. **D83** (2011) 014018
16. LHCb collaboration, CERN-LHCb-CONF-2017-002